



# Effect of temperature disturbance on end-gas autoignition and detonation development

Linlin Yang<sup>a</sup>, Yiqing Wang<sup>a,\*</sup>, Peng Dai<sup>b</sup>, Zheng Chen<sup>a</sup>

<sup>a</sup> HEDPS, SKLTCS, College of Engineering, Peking University, Beijing 100871, China

<sup>b</sup> Department of Mechanics and Aerospace Engineering, Southern University of Science and Technology, Shenzhen 518055, China

## ARTICLE INFO

### Keywords:

End-gas autoignition  
Detonation development  
Temperature disturbance  
Hydrogen

## ABSTRACT

Knocking is one of the main constraints in improving the thermal efficiency of spark ignition engines. It is generally accepted that normal knock and super-knock are respectively caused by autoignition and detonation development in end-gas. In this study, the effect of temperature disturbance on end-gas autoignition and detonation development in a closed circular domain is examined through 2D simulations considering detailed chemistry. In simulations we find typical end-gas combustion modes including triple-detonation, double-detonation and double-tongue structures, which were also observed in previous rapid compression machine (RCM) experiments. It is shown that the detonation development in end-gas is very sensitive to the temperature disturbance,  $\Delta T$ . As  $\Delta T$  increases, the first autoignition in end-gas induced by temperature disturbance occurs earlier while the corresponding pressure wave is weaker, which subsequently results in different combustion modes in end-gas. Specifically, for small  $\Delta T$ , a supersonic autoignition is initiated and then it triggers a triple-detonation structure consisting of a radial detonation induced by shock-flame coupling and two circumferential detonations that are caused by the near-wall shock compression induced detonation (NWSCD) mechanism. For moderate  $\Delta T$ , the radial detonation is suppressed due to the earlier first autoignition and weaker pressure waves, and thereby the double-detonation structure consisting of two circumferential detonations appears. These two detonations are formed through near wall autoignition induced detonation (NWAID) mechanism. For relatively large  $\Delta T$ , there is no detonation development since the end-gas is quickly consumed by autoignition, which results in a double autoignition front structure, referred to as the double-tongue structure. In this study, the formation of complicated autoignition and detonation structures is interpreted. The results provide insight in understanding the development of normal knock and super-knock in spark ignition engines.

## 1. Introduction

Recently, hydrogen-fueled internal combustion engines (ICEs) have received great attention since hydrogen is a carbon-free alternative fuel [1]. Since knocking is one of the main constraints in improving the thermal efficiency of spark ignition engines [2], it is important to understand the mechanisms of knock onset in hydrogen-fueled ICEs.

It is generally accepted that engine knock is mainly caused by end-gas autoignition [3]. When premixed flame propagates in a closed chamber, the end-gas is progressively compressed and its temperature and pressure continuously increase. Under certain conditions, autoignition happens to end-gas before it is completely consumed by the propagating flame front. When the local autoignition couples coherently with pressure waves induced by itself, detonation may develop, which

results in the so-called super-knock [2]. The super-knock can induce extremely large pressure oscillation (above 200 atm) and cause severe damage to engines. Therefore, we need prevent super-knock/detonation development in H<sub>2</sub>-fueled ICEs.

In the literature, there are many studies on end-gas autoignition and detonation development. Based on the reactivity gradient theory of Zel'dovich [4], Bradley and co-workers [5,6] categorized end-gas combustion into five modes according to the normalized temperature gradient,  $\xi$ , which equals the ratio of the local sound speed to the autoignitive reaction front propagation speed, i.e.,  $\xi = a/u_a$ . Small value of  $\xi$  corresponds to the supersonic autoignition while large  $\xi$  leads to deflagration mode. When  $\xi$  is close to unity, the chemical reaction and pressure wave strongly couple with each other, resulting in detonation development. Dai et al. [7] found that for large hydrocarbon fuels, both

\* Corresponding author.

E-mail address: [wangyiqing@pku.edu.cn](mailto:wangyiqing@pku.edu.cn) (Y. Wang).

<https://doi.org/10.1016/j.proci.2024.105220>

Received 2 December 2023; Accepted 29 May 2024

1540-7489/© 2024 The Combustion Institute. Published by Elsevier Inc. All rights are reserved, including those for text and data mining, AI training, and similar technologies.

hot spots and cool spots can lead to detonation development in the end-gas. Besides, the detonation development was studied for different fuels, diluents, thermal conditions, and geometries via 1D (see [8–11] and references therein) and multi-dimensional simulations (e.g., [12, 13]).

However, the above studies [5–13] did not take into account multi-dimensional wave interaction, which may have a significant impact on end-gas autoignition and detonation development. Wang et al. [14–16] studied the detonation development/super-knock under engine-relevant conditions using the rapid compression machine (RCM). In their experiments, detonation development was recorded via high-speed visualization. Using the recorded images and pressure traces, they [14] demonstrated that the deflagration-to-detonation transition can be triggered by a hot spot-induced preignition in the end-gas. Fig. 1 (a) shows the triple-detonation structure observed in their experiments [14]. Since detonation development and propagation are extremely fast, only a few images can be recorded in experiments. Consequently, the formation and subsequent propagation of triple-detonation structure were not well understood. Besides, other end-gas combustion modes including double-detonation (see Fig. 1b) and double-tongue reaction front (see Fig. 1c) were observed in RCM experiments [15,16]. Wang et al. [17] proposed that the detonation development appearing in the near-wall region is mainly induced by shock wave reflection on the wall. However, the underlying mechanism for detonation development is still not well understood since limited information (e.g., high-speed image and pressure trace) can be obtained in experiments. This motivates the present study, which investigates different combustion modes in end-gas induced by a hot spot in a circular domain using high-fidelity 2D simulations.

The objectives of this work are to assess the effects of temperature disturbance on the combustion modes in end-gas and to interpret the mechanism of detonation development. We consider the premixed hydrogen/air flame propagation from the center of a 2D, closed, circular domain, in which there is a hot spot appearing near the wall. By simply changing the temperature disturbance of the hot spot, different end-gas combustion modes can be observed and analyzed.

## 2. Numerical model and methods

We consider a 2D, closed, circular domain initially filled with static, stoichiometric hydrogen/air mixture at  $T_0=1000$  K and  $P_0=10$  atm. Note that in this study hydrogen is considered instead of hydrocarbons that were used in previous experiments depicted in Fig. 1. The initial conditions of premixed  $H_2$ /air mixture are based on previous study [18]. The central ignition results in a circular expanding flame. Due to symmetry, the computational domain in Fig. 2 is a semicircle in the radius of 2 cm. Symmetry boundary condition is imposed on the line at  $y = 0$ , while adiabatic wall boundary condition is used for  $r = 2$  cm. Although the thermo-diffusive and hydrodynamic instabilities developed on the flame front can break the symmetry, it is expected that the end-gas autoignition and detonation modes are almost unaffected by the symmetry break-up because they are dominated by the temperature nonuniformity in the unburnt region.

To trigger end-gas autoignition and detonation development, we

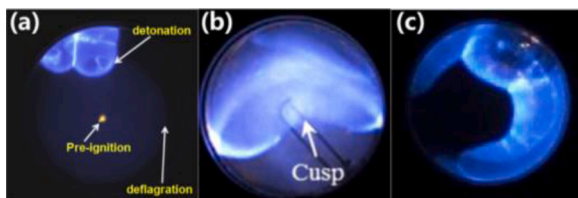


Fig. 1. Different end-gas combustion modes observed in previous experiments: (a) triple-detonation [14], (b) double-detonation [15] and (c) double-tongue reaction front [16].

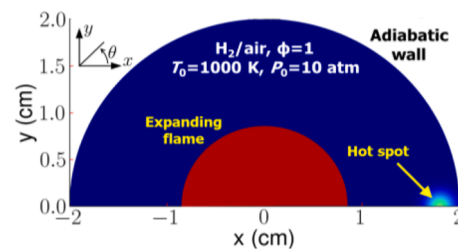


Fig. 2. Schematic of flame propagation in a circular computational domain. There is a near-wall hot spot with  $T_0+\Delta T$  in the end-gas.

impose a hot spot near the wall (see Fig. 2). The temperature distribution of the hot spot is:

$$T = T_0 + \Delta T \exp\left\{-\left[(x-x_0)^2 + y^2\right]/(r_H^2)\right\} \quad (1)$$

with  $x_0=1.8$  cm and  $r_H=0.1$  cm. We consider three values of temperature disturbance,  $\Delta T=10$  K, 30 K and 50 K, referred to as T10, T30 and T50, respectively. To reproduce experimental phenomena in Fig. 1, the three temperature disturbance values within the range of 10 ~50 K, which aims to mimic the temperature inhomogeneity in ICEs [2,19], were tested and selected. The values of  $\xi$  for  $\Delta T=10$  K, 30 K and 50 K are 48, 88 and 90, respectively. Therefore, the end-gas autoignition mode for T10 could be different from that for T30 and T50. Note that the end-gas combustion mode for T30 and T50 could be different since it is also strongly affected by the complex interaction among flame front, wall and the pressure waves generated by end-gas autoignition, which makes the end-gas combustion mode sensitive to the temperature disturbance.

The fully compressible Navier-Stokes solver for a multi-component reactive flow, *PeleC* [20], is used in this work. In *PeleC*, the finite volume method is used and a second-order explicit method is employed for time-stepping. The shock capturing scheme is the method of line approach with characteristic extrapolation to cell faces. Moreover, adaptive mesh refinement based on the gradients of temperature and pressure, and the mass fraction of H radical is used to accurately and efficiently resolve the propagating reaction front and shock wave. The detailed kinetic model for hydrogen by Konnov [21] is adopted and the mixture-averaged transport model is used. *PeleC* has been successfully used in previous studies on end-gas autoignition [22] and detonation [23]. The details on numerical methods and code validation can be found in [20] and thereby are not repeated here. In all simulations, the maximum mesh level is five and the minimum mesh size is 1.23  $\mu\text{m}$ . The laminar flame thickness and the reaction induction length at the thermodynamic condition of end-gas right before the occurrence of autoignition (i.e., 1200 K and 20 atm) are 29 and 125  $\mu\text{m}$ , respectively. Such fine mesh is used to ensure that grid-independence is achieved (see Supplementary Material) and that the expanding circular flame, autoignition front and detonation are well-resolved. The a posteriori study from our simulations also shows that there are about 20 points and 8 points within the flame thickness and the detonation half reaction thickness, respectively. Previous studies [23,24] have shown that a minimum of 5 points in the heat releases zone can ensure the grid-independent results of the detonation structure. Therefore, both detonation wave and the flame front are well resolved throughout our simulations.

## 3. Results and discussion

### 3.1. Different combustion modes in end-gas

Fig. 3 shows contour of temperature and density gradient at four instants for each case. The central ignition induces a circular expanding flame (CEF) propagating outwardly. The front of the CEF is not smooth and cellular flame structure is observed. This is caused by the

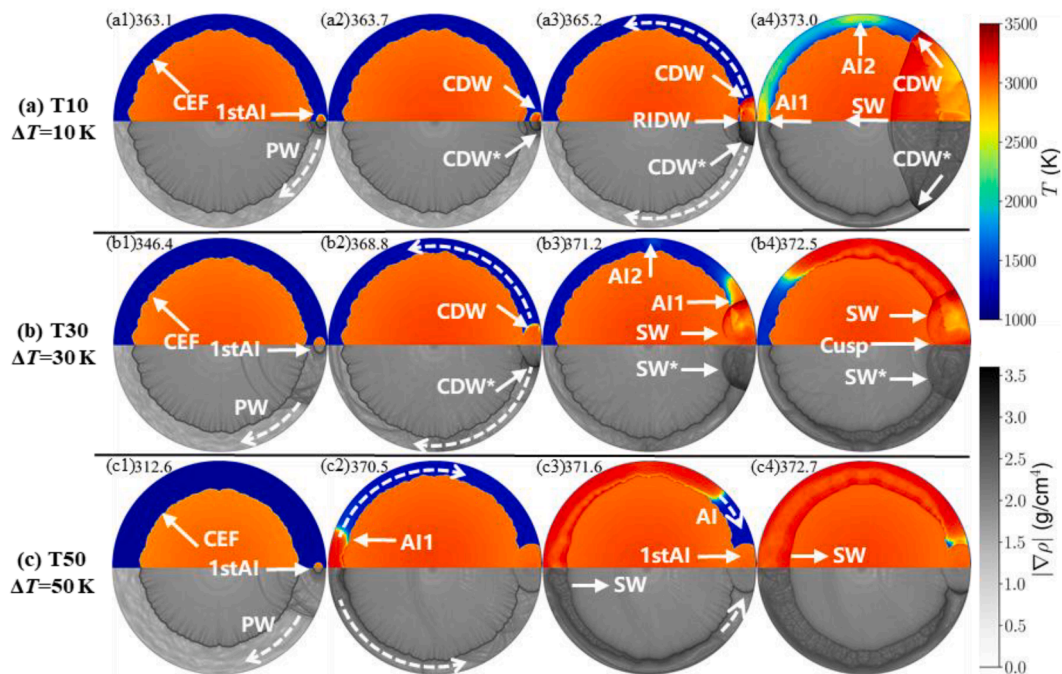


**Fig. 3.** Contour of temperature and density gradient at four instants (in the unit of microsecond) during the end-gas combustion for  $\Delta T=10$  K (top), 30 K (middle) and 50 K (bottom). The radius of circular domain is 2 cm. CEF: circular expanding flame; AI: autoignition; CDW: circumferential detonation wave; RIDW: radial detonation wave; SW: shock wave; PW: pressure wave. The symbol "\*" denotes that the detonation/shock wave is in the symmetry plane and is not simulated.

hydrodynamic instability which is more severe at higher pressure. Before the occurrence of end-gas combustion, the CEF is similar for T10, T30 and T50. Inside the closed circular domain, the CEF is like a piston which compresses the end-gas. Consequently, the temperature and pressure of the end-gas increase gradually. Since the temperature of the hot spot center near the wall is slightly higher than that of the surrounding mixture, end-gas autoignition first occurs there. Fig. 3(a1) shows that the first autoignition, 1stAI, occurs at around  $t = 363.1 \mu\text{s}$  for  $\Delta T=10$  K. As temperature disturbance increases, the 1stAI occurs earlier as expected:  $t = 346.4 \mu\text{s}$  for  $\Delta T=30$  K in Fig. 3(b1) and  $t = 312.5 \mu\text{s}$  for  $\Delta T=50$  K in Fig. 3(c1). The sudden heat release from the 1stAI produces pressure waves as shown by the contours for density gradient in Figs. 3(a1, b1, c1). These pressure waves propagate into and compress the surrounding end-gas, which results in further increase in temperature and pressure. Moreover, these pressure waves interact with the CEF and wall, respectively on the left and right sides, and thereby affect the subsequent end-gas combustion modes.

After the occurrence of 1stAI, different end-gas combustion modes are observed for  $\Delta T=10$  K, 30 K and 50 K. For the case T10 with  $\Delta T=10$  K, shortly after the 1stAI front reaches the wall, at  $t = 363.7 \mu\text{s}$  two circumferential detonation waves, CDW and CDW\* in Fig. 3(a2), form near the wall and propagate in the opposite circumferential directions. Then as shown in Fig. 3(a3), these two CDWs propagate in the end-gas along the near-wall region. Meanwhile, the leftward propagating detonation wave decays into a pressure wave due to the lack of reactants, which will come up with the leading autoignition front and evolve into the third detonation wave propagating inwardly toward the CEF along the radial direction. This radial-inward detonation wave is denoted as RIDW, as shown in Fig. 3(a3). This triple-detonation structure, consisting of CDW, CDW\* and RIDW, is similar to that observed in previous experiments [14] (see Fig. 1a). More details of these processes will be discussed in Section 3.2. When the RIDW collides with the CEF, it decays to a shock wave (SW in Fig. 3(a4)) since the reactants in front of the RIDW have been consumed by the CEF. However, unburned reactants still remain in the annular region near the wall. Therefore, CDW and CDW\* both propagate in a rotating manner. At around  $t = 373.0 \mu\text{s}$ , Fig. 3(a4) shows that autoignition AI1 occurs at  $\theta \approx \pi$  and AI2 appears at

$\theta \approx \pi/2$ . Since the autoignition front propagates at much higher speed than CDW and CDW\*, the residual end-gas is consumed in a short interval by AI.

For the case T30 with  $\Delta T=30$  K, two circumferential detonation waves, CDW and CDW\*, are also observed in Fig. 3(b2). However, the end-gas combustion mode for T30 is different from that for T10. There are mainly three differences between T10 and T30. First, for T30 the CDWs do not appear immediately after the 1stAI front reaches the wall. By comparing Figs. 3(a2) and 3(b2) with Figs. 3(a1) and 3(b1), it is seen that for T30 case, the 1stAI occurs much earlier while it develops into the CDW at the almost same instant compared with T10. Therefore, it is clear that the transition from the 1stAI to CDW takes a longer time in the case of T30 compared to T10. The second difference is that in the radial direction there is no detonation wave. Fig. 3(b3) shows that two oblique shock waves, SW and SW\*, propagate in the burnt region together with CDW and CDW\*. This is similar to the continuously rotating detonation wave structure [25]. Besides, the double-detonation structure in Fig. 3(b3) is similar to the cusp-like structure observed in previous experiments [15] (see Fig. 1b). The third difference is that autoignition AI1 occurs in the unburned gas near the detonation front (see Fig. 3(b4) for T30) rather than at the farthest position,  $\theta = \pi$ , from the detonation front (see Fig. 3(a4) for T10).

The end-gas combustion for case T50 is quite different from those for cases T10 and T30. Fig. 3(c) shows that after the 1stAI occurring at the hot spot near the right wall, no detonation development is observed. Fig. 3(c1) shows that the pressure waves induced by the 1stAI propagate circumferentially in the end-gas along the wall. Finally, strong collision between pressure waves occurs at  $\theta = \pi$ , which results in AI1 near the left wall around  $t = 370.5 \mu\text{s}$ , as shown in Fig. 3(c2). The AI1 fronts propagate at extremely high speed in the circumferential directions. Consequently, the double-tongue reaction front is observed in Fig. 3(c3), which is similar to that observed in previous experiments [16] (see Fig. 1c). Fig. 3(c) shows that all the reactants are consumed by the AI fronts within  $3 \mu\text{s}$  and there is no detonation development.

It is noted that in Fig. 3, new AI prefers to occur at the position of  $\theta \approx 0, \pi/2$  or  $\pi$ . This is because strong pressure wave reflection or collision happens at these locations. Such observation and explanation were also

reported by Wang et al. [17].

To quantify different combustion modes in the end-gas, we calculate the propagation speed of reaction front for both AI and CDW. Specifically, the propagation history of the reaction front along the circle with radius of  $r = 1.95$  cm is first recorded. Then the propagation speed is obtained from linear fitting between the reaction front position and time. Note that during the propagation of reaction front, the relation between distance that the reaction front has travelled, and time is almost linear, which is presented in the Supplementary Material. Therefore, the linear fitting method which was used in previous studies [15,17] is also used here to determine the propagation speed of the autoignition and detonation fronts. The results for different stages of cases T10, T30 and T50 are listed in Table 1. It is seen that for T10, the reaction front speed of the 1stAI is around 1080 m/s, which is much higher than those for T30 and T50. Note that the sound speed in the end-gas (which is at  $T = 1200$  K and  $P = 2.06 \times 10^6$  Pa at the moment before 1stAD) is around  $a = 800$  m/s. Therefore, the 1stAI front propagates at supersonic speed for case T10 while subsonic propagation happens to the 1stAI front for cases T30 and T50. This is due to the fact that the reaction front speed is inversely proportional to the temperature gradient according to the reactivity gradient theory of Zel'dovich [4–6]. The smaller value of  $\Delta T$  leads to lower temperature gradient and thereby higher reaction front speed. The detonation speed for CDW is around 1960 m/s and 2000 m/s for T10 and T30, respectively. They are very close to the C-J detonation speed of the end-gas (the relative difference is within 1.5 %). This is reasonable since the width of the unburnt region is small, and the circle ( $r = 1.95$  cm) used to calculate the propagation speed is close to the wall, as explained in previous studies [26,27]. Besides, the AI front speeds for T30 and T50 are both above 20,000 m/s, which is one-order higher than the detonation speed. Therefore, the residual unburned gas is almost immediately consumed by the AI fronts. Note that for case T10, multiple AI fronts appear in the unburnt region which instantaneously consume the unburned gas; fast chemical reaction almost occurs in the whole space in end-gas, as shown in Fig. 3(a4). It is difficult to distinguish a propagating reaction front. Therefore, the speed is not calculated.

To further quantify different combustion modes in the end-gas, we record and compare the pressure history for T10, T30 and T50. Specifically, the near-wall pressure history at ( $x = 1.99$  cm,  $y = 0$  cm) for T10 and T30 and that at ( $x = -1.99$  cm,  $y = 0$  cm) for T50 are shown in Fig. 4(a). The evolution of maximum pressure within the whole domain is plotted in Fig. 4(b). Note that at  $t = 0.35$  ms, the near-wall pressure is close to 20 atm, which is much higher than the initial pressure  $P_0 = 10$  atm. Such pressure rise is due to continuously compression of the end-gas by the CEF in the closed chamber. The evolution of near-wall temperature and pressure for case T10 provided in the Supplementary Material clearly demonstrates the compression process. For  $\Delta T = 10$  K, Fig. 4(a) shows that there is a noticeable pressure spike induced by the 1stAI at around  $t = 0.362$  ms, which is not observed for  $\Delta T = 30$  K and 50 K. This indicates that the pressure wave generated by the supersonic 1stAI for  $\Delta T = 10$  K is much stronger than those by subsonic 1stAI for  $\Delta T = 30$  K and 50 K. This is crucial to the subsequent end-gas combustion because strong interaction between pressure wave and autoignition is prone to induce detonation.

When detonation develops, the peak pressure increases dramatically and is much higher than that after autoignition. Therefore, Fig. 4(b) shows that peak pressure can be above 300 atm for  $\Delta T = 10$  K and 30 K with detonation development, while it is around 50 atm for  $\Delta T = 50$  K in which only end-gas autoignition occurs and there is no detonation

**Table 1**

Reaction front speeds at different stages for T10, T30, T50.

$\Delta T$	10 K	30 K	50 K
1stAI speed, $u_a$ (m/s)	1080	100	60
CDW speed, $u_D$ (m/s)	1960	2000	N/A
AI speed, $u_a$ (m/s)		22,400	21,200

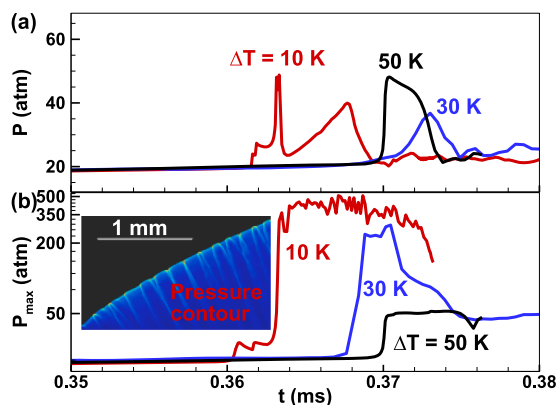


**Fig. 4.** Evolution of (a) the near-wall pressure and (b) the maximum pressure for  $\Delta T = 10$  K, 30 K and 50 K. The insert shows the pressure contour of the detonation front for  $\Delta T = 10$  K.

development. The insert in Fig. 4(b) shows the cellular structure of the detonation front, and the peak pressure appears at the triple point which is the intersection among the transverse wave, incident shock and Mach stem. Comparison between Figs. 4(a) and 4(b) indicates that due to detonation development in end-gas, the pressure inside the chamber can be much higher than that near the wall. According to Wang et al., [2], super-knock is characterized by overpressure above 20 MPa. Therefore, super-knock occurs for cases T10 and T30, while conventional knock happens for case T50.

The above results indicate that detonation development and knock intensity are very sensitive to the temperature disturbance in end gas. To reveal the underlying mechanisms for different combustion modes induced by temperature disturbance, we conduct detailed analysis on the reaction front for each case in following subsections.

### 3.2. Detonation development for $\Delta T = 10$ K

As shown in Fig. 3(a), the triple-detonation structure consisting of CDW, CDW\* and RIDW is formed for case T10 with  $\Delta T = 10$  K. To explain the mechanism for the formation of CDW shortly after the 1stAI front reaches the wall, in Fig. 5 we plot the temperature and pressure profiles along the symmetry line (i.e.,  $y = 0$ ) during the process of the 1stAI front approaching the wall.

Fig. 5 shows that at  $t = 361.4$   $\mu$ s (line #1), the shock wave generated by the 1stAI propagates toward the right wall. Then it is reflected on the wall (see line #2) which further compresses the end-gas. This leftward-

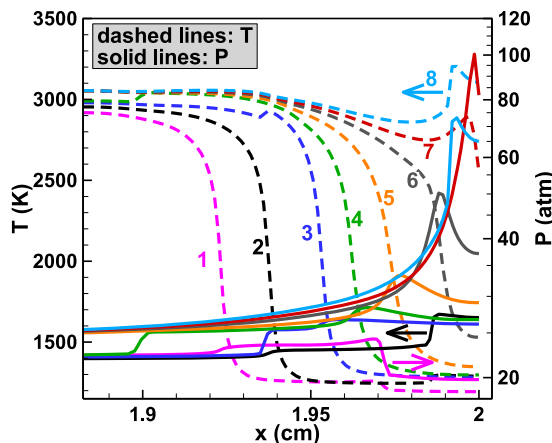


**Fig. 5.** Evolution of the temperature and pressure profiles along the symmetry line (i.e.,  $y = 0$ ). The time sequence is: #1: 361.4  $\mu$ s, #2: 361.9  $\mu$ s, #3: 362.5  $\mu$ s, #4: 362.8  $\mu$ s, #5: 363.0  $\mu$ s, #6: 363.16  $\mu$ s, #7: 363.23  $\mu$ s, #8: 363.28  $\mu$ s.

propagating reflected shock wave moves toward and collides with the rightward-propagating 1stAI front, producing a transmissive wave propagating to the left burnt region and a rightward-propagating reflected wave that begins to couple with the 1stAI front (see line #3). As shown by lines #4~#6, the coupling between the 1stAI front and pressure wave further enhances the pressure wave. Finally, a detonation wave develops in the near-wall region which consumes the end-gas therein. Similar detonation development process was reported in Fig. 14 of [18] and can be well explained by the reactivity gradient theory of Zel'dovich [4] and the SWACER mechanism of Lee et al. [28]. At  $t = 362.23 \mu\text{s}$  (line #7), the peak pressure is above 100 atm. Since there is no unburnt gas left for the detonation, the peak pressure decays to around 75 atm (line #8).

Though the lifetime of the above near-wall detonation development shown in Fig. 5 is very short, it is crucial to the formation of CDWs since it generates a strong shock wave near the wall. It is noted that the unburnt end-gas has very high reactivity after it is compressed to high temperature and pressure by the CEF. This shock wave propagates in the circumferential directions and further compresses the surrounding unburnt end-gas, resulting in two circumferential detonation waves, CDW and CDW\*, as shown in Fig. 3(a2). Therefore, the CDWs observed in case T10 are referred to as the near-wall shock compression induced detonation (NWSCD). This mechanism requires a strong shock wave. In case T10, the strong shock is generated through two processes: first the supersonic 1stAI generates initial shock; and then the initial shock induces the near-wall detonation which forms the shock after it consumes the unburnt gas near the wall.

Fig. 6 depicts the formation of radial detonation front (RIDW) shown in Fig. 3(a3). The temperature contours near the 1stAI are plotted for four instants on the top of Fig. 6. At  $t = 364.9 \mu\text{s}$  (line and sub-figure #1), the pressure wave (line #8 in Fig. 5) is on the right side of the 1stAI front. This pressure wave is enhanced by the 1stAI front at  $x = 1.695 \text{ cm}$  (line #2 in Fig. 6). Due to coherent coupling between chemical reaction and pressure wave, the pressure wave intensity continues to increase and finally detonation development happens (see lines #2, #3 and #4). The RIDW decays to a strong shock wave after it propagates into the burnt region (line #5).

As mentioned before, the triple-detonation structure in case T10, Fig. 3(a3), is similar to the experimental result, Fig.1(a), reported by Wang et al. [14]. In their study, the very strong pressure oscillation was attributed to this near-wall triple-detonation structure. They proposed that the triple-detonation structure could be induced by three explosion centers near the wall [14,15]. However, the above simulation results

show that the near-wall triple-detonation structure can be induced by a single hot spot in the near-wall region.

### 3.3. Detonation development for $\Delta T=30 \text{ K}$

Unlike the case with  $\Delta T=10 \text{ K}$ , there is no RIDW for the case with  $\Delta T=30 \text{ K}$ . This is because detonation development does not happen at relatively large temperature gradient according to the reactivity gradient theory [4–6]. As shown in Table 1, for  $\Delta T=30 \text{ K}$  the speed of the 1stAI front is around 100 m/s, which is about one order of magnitude smaller than the sound speed of unburned gas, 800 m/s. Therefore, the pressure wave cannot couple with the 1stAI front and thereby there is no detonation development directly induced by the 1stAI. Moreover, the pressure wave generated by the 1stAI is much weaker for  $\Delta T=30 \text{ K}$  than that for  $\Delta T=10 \text{ K}$ . Consequently, it is difficult to achieve transition to detonation in the radial direction through the NWSCD mechanism. Furthermore, the unburnt gas region between the 1stAI and CEF is small, and thereby the unburnt mixture is completely consumed before potential RIDW or AI occurs. The above factors make the 1stAI front unable to evolve into a RIDW for  $\Delta T=30 \text{ K}$ .

Similar to the case with  $\Delta T=10 \text{ K}$ , the CDWs are also observed in the case with  $\Delta T=30 \text{ K}$ . However, the mechanism for CDW formation is different. Specifically, it is the near-wall autoignition induced detonation (NWAID) that leads to the formation of CDWs for  $\Delta T=30 \text{ K}$ . Fig. 7 shows the distributions of temperature and pressure profiles in the circumferential direction (along the near-wall circle with  $r = 1.99 \text{ cm}$ ). From  $t = 366.02 \mu\text{s}$  to  $t = 366.83 \mu\text{s}$  (lines #1 and #2), the near-wall 1stAI front propagates subsonically with nearly uniform pressure distribution. However, at  $t = 367.64 \mu\text{s}$  (line #3), the temperature and pressure of the unburned gas in the region of  $0.13 < \theta < 0.15$  both rise due to the chemical reaction occurring there. At  $t = 368.42 \mu\text{s}$  (line #4), the pressure rise in the mixture before the reaction front is above 20 atm, indicating that strong autoignition happens there. Finally, at  $t = 368.82 \mu\text{s}$  (line #5) a shock wave is shown to be developed and coupled with the reaction front, indicating that the detonation forms. The density gradient contour #5 clearly shows there is an autoignition kernel appearing in the near-wall region. The AI kernel is enclosed within a box where the density gradient differs from the surrounding due to reaction. Therefore, the CDW observed for  $\Delta T=30 \text{ K}$  is caused by the NWAID mechanism. Note that the NWAID was also observed in the experiments by Qi et al. [15].

In case T10, CDW happens immediately after the 1stAI (see Figs. 3(a1) and 3(a2)). However, Figs. 3(b1) and 3(b2) show that for T30 CDW is postponed. This is because the earlier 1stAI for T30 results in relatively

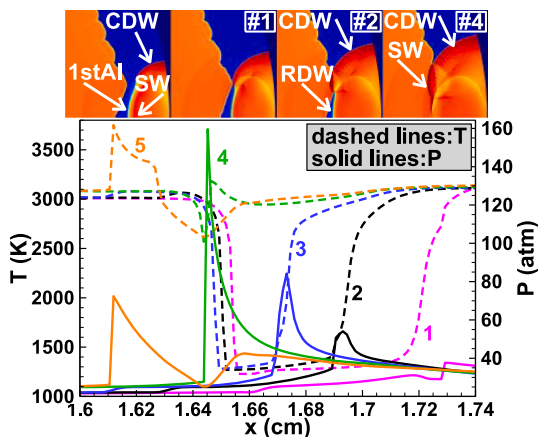


Fig. 6. Evolution of the temperature and pressure profiles along the symmetry line at  $y = 0$  during the formation of RIDW and triple-detonation structure for case T10. The top figures are four representative temperature contours. The time sequence is: #1:  $364.9 \mu\text{s}$ , #2:  $365.2 \mu\text{s}$ , #3:  $365.3 \mu\text{s}$ , #4:  $365.5 \mu\text{s}$ , #5:  $365.6 \mu\text{s}$ .

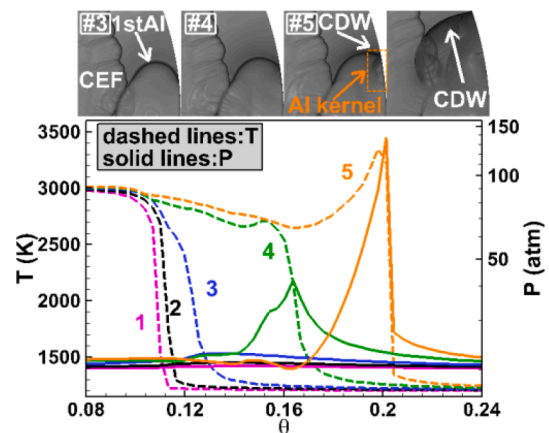


Fig. 7. Evolution of the temperature and pressure profiles along the circle in the radius of  $r = 1.99 \text{ cm}$ . The top figures are density gradient contours during the CDW formation. The time sequence is: #1:  $366.02 \mu\text{s}$ , #2:  $366.83 \mu\text{s}$ , #3:  $367.64 \mu\text{s}$ , #4:  $368.42 \mu\text{s}$ , #5:  $368.82 \mu\text{s}$ .

weaker compression of the end-gas and thereby produces relatively weaker pressure wave. Consequently, CDW cannot develop immediately after the 1stAI for T30. This further demonstrates that detonation development is very sensitive to the temperature disturbance of the hot spot in end-gas.

### 3.4. Autoignition for $\Delta T=50$ K

Unlike the cases of  $\Delta T=10$  and 30 K, there is no detonation development for  $\Delta T=50$  K. To explain why detonation doesn't occur, in Fig. 8 we plot the contour of ignition delay time  $\tau$  and normalized temperature gradient  $\xi$  at the moment immediately before AI happens (see Fig. 3 (c2)). The ignition delay time is calculated using the 0D homogenous constant-pressure reactor model at each grid cell. Note that the similar results are obtained when the constant-volume reactor is used, as shown in the Supplementary Material. It is seen that the ignition delay time  $\tau$  increases gradually from  $\tau=3 \times 10^{-7}$  s on the left side with  $\theta=\pi$  to  $\tau=3 \times 10^{-6}$  s at the 1stAI front with  $\theta \approx \pi/10$ . In the end-gas, the normalized temperature gradient is much smaller than unity. This indicates that supersonic propagation of autoignition front since  $\xi=a/u_d$  [5,6]. Though  $\xi \approx 1$  occurs in near the 1stAI front with  $\theta \approx \pi/10$ , the ignition delay time there is much longer than that at  $\theta=\pi$ . Therefore, before detonation development near the 1stAI front, autoignition already happens and consumes all the end-gas.

The propagation of the supersonic AI front in the circumferential direction is shown in Fig. 9. At  $t = 331.8 \mu\text{s}$  (line #1), only 1stAI exists near  $\theta=0$  and the pressure is nearly uniform. At  $t = 369.9 \mu\text{s}$  (line #2), the pressure and temperature around  $\theta=\pi$  start to increase due to the collision and reflection of the pressure waves generated by the 1stAI. Therefore, autoignition AI1 starts at  $\theta=\pi$  and propagates towards  $\theta=0$ , as also shown by Fig. 3(c2). A new autoignition kernel, AI2, appears around  $\theta=1.1$  at  $t = 371.2 \mu\text{s}$  (line #5). Note that the AI2 is not shown in Fig. 3 since it only exists for a relatively short interval and then merges quickly with the AI1. These two AI fronts merge into one AI front (line #9 and also the AI in Fig. 3(c3)) and form a double-tongue structure that propagates towards the 1stAI front until all the reactants are consumed, as shown in Fig. 3(c4).

Fig. 10 explains the formation of AI2. To better visualize the pressure waves in the end-gas, the contour of volumetric dilatation ( $\nabla \cdot \mathbf{u}$ ) is used. It is seen that the AI2 is caused by the pressure wave reflection in the ring-shaped unburnt region. Since the domain is circular, pressure waves caused by the 1stAI kernel propagate outwardly, and then are reflected by the curved wall, enhancing the reactivity of the unburnt gas at around  $\theta=1.1$  and leading to the autoignition kernel AI2.

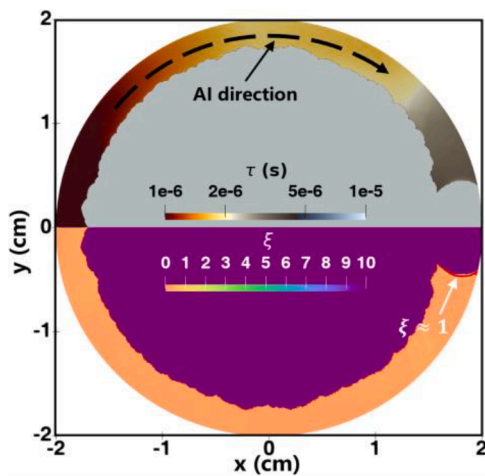


Fig. 8. Contour of ignition delay time,  $\tau$  (upper) and normalized temperature gradient,  $\xi$  (bottom) at  $t = 369.8 \mu\text{s}$ . Regions with  $0.8 < \xi < 1.2$  are covered by red color. The burnt region is in grey (upper) and purple (bottom).

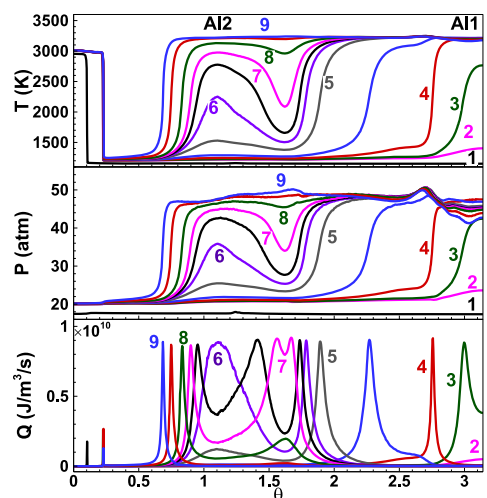


Fig. 9. Temporal evolution of temperature, pressure and heat release rate distributions along the circle in the radius of  $r = 1.99$  cm for  $\Delta T=50$  K. The time sequence is: #1: 331.8  $\mu\text{s}$ , #2: 369.9  $\mu\text{s}$ , #3: 370.1  $\mu\text{s}$ , #4: 370.5  $\mu\text{s}$ , #5: 371.2  $\mu\text{s}$ , #6: 371.3  $\mu\text{s}$ , #7: 371.4  $\mu\text{s}$ , #8: 371.5  $\mu\text{s}$ , #9: 371.9  $\mu\text{s}$ .

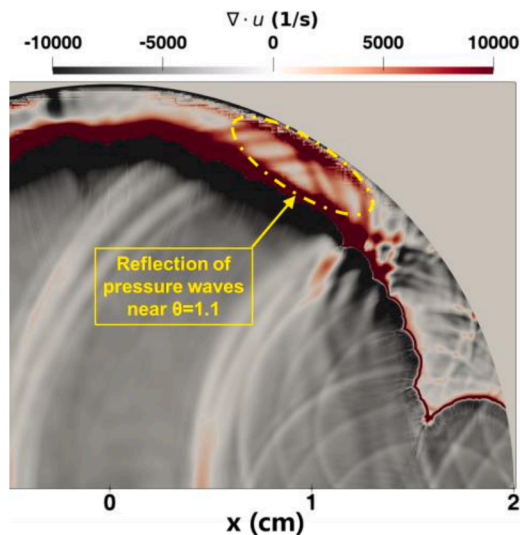


Fig. 10. Contour of volumetric dilatation at the instant immediately before AI2 happens ( $t = 371.2 \mu\text{s}$ , Line#5 in Fig. 9) for  $\Delta T=50$  K.

## 4. Conclusions

The effect of temperature disturbance on end-gas autoignition and detonation development in a closed circular domain is examined using 2D simulations. Three temperature disturbances of  $\Delta T=10$  K, 30 K and 50 K are considered for a hot spot in end-gas of stoichiometric hydrogen/air initially at  $T_0=1000$  K and  $P_0=10$  atm. Typical end-gas combustion modes including triple-detonation, double-detonation and double-tongue structures observed in previous RCM experiments [14–16] are reproduced in our simulations and their formation mechanisms are interpreted.

It is shown that detonation development in end-gas is very sensitive to the temperature disturbance,  $\Delta T$ , of the hot spot. Detonation development is observed for  $\Delta T=10$  K and 30 K but not for  $\Delta T=50$  K. For  $\Delta T=10$  K, the triple-detonation structure consisting of two circumferential detonation waves, CDW and CDW\*, and one radial detonation wave (RIDW) is caused by near-wall shock compression induced detonation (NWSKD) and shock-flame coupling. Strong pressure wave generated by the 1stAI induces coherent coupling between chemical

reaction and pressure wave and thereby detonation development. For  $\Delta T=30$  K, since the pressure wave caused by the 1stAI is relatively weak, there is no RIDW. Though two CDWs are also observed, they are near-wall autoignition induced detonation (NWAID) rather than NWSGD. For  $\Delta T=50$  K, the autoignition front propagates much faster than the sound speed. Therefore, the end-gas is totally consumed by autoignition after the 1stAI happens, and there is no detonation development.

Note that the effect of turbulent flow in engines is not considered here and needs to be explored in future studies. Nevertheless, the present results are still useful as a first step towards an understanding of the complicated detonation development, especially that observed in previous RCM experiments.

### Novelty and significance statement

This study provides novel insights into end-gas autoignition and detonation development. The mechanisms for the formation of triple-detonation, double-detonation, and double-tongue structures are interpreted for the first time through two-dimensional simulations considering detailed chemistry. The primary role of first autoignition is highlighted and its influence on subsequent end-gas combustion modes is assessed. It is shown that the detonation development in end-gas is very sensitive to the temperature disturbance.

The results are significant because normal knock and super-knock, respectively caused by autoignition and detonation development, are the main constraints in improving the thermal efficiency of spark ignition engines. However, their initiation process for autoignition and detonation is difficult to be captured in experiments and is not well understood. With the help of high-fidelity 2D simulations, we clearly interpret the mechanisms for detonation development at different temperature disturbances. We find that different temperature disturbances significantly affect first autoignition and pressure wave intensity, and thereby affect the subsequent detonation development.

### Author Contributions

- Linlin Yang: performed the research, analyzed data, and drafted the manuscript.
- Yiqing Wang: designing the paper structure, aided in interpreting the results, and revised the manuscript.
- Peng Dai: aided in interpreting the results and revised the manuscript.
- Zheng Chen: designed the research, supervised the project, and revised the manuscript.
- All authors discussed the results and contributed to the final manuscript.

### Declaration of competing interest

The authors declare that they have no known competing financial interests or personal relationships that could have appeared to influence the work reported in this paper.

### Acknowledgements

This work was funded by NSFC, China (Nos. 521760965 and 51861135309).

### Supplementary materials

Supplementary material associated with this article can be found, in the online version, at [doi:10.1016/j.proci.2024.105220](https://doi.org/10.1016/j.proci.2024.105220).

### References

- [1] A. Onorati, R. Payri, B. Vaglieco, A. Agarwal, C. Bae, G. Bruneaux, M. Canakci, M. Gavaises, M. Günthner, C. Hasse, S. Kokjohn, S.-C. Kong, Y. Moriyoshi, R. Novella, A. Pesyridis, R. Reitz, T. Ryan, R. Wagner, H. Zhao, The role of hydrogen for future internal combustion engines, *Int. J. Engine Res.* 23 (2022) 529–540.
- [2] Z. Wang, H. Liu, R.D. Reitz, Knocking combustion in spark-ignition engines, *Prog. Energy Combust. Sci.* 61 (2017) 78–112.
- [3] J.B. Heywood, *Internal Combustion Engine Fundamentals*, McGraw-Hill, New York, 1988.
- [4] Y. Zeldovich, Regime classification of an exothermic reaction with nonuniform initial conditions, *Combust. Flame* 39 (1980) 211–214.
- [5] X.J. Gu, D.R. Emerson, D. Bradley, Modes of reaction front propagation from hot spots, *Combust. Flame* 133 (2003) 63–74.
- [6] D. Bradley, C. Morley, X.J. Gu, D.R. Emerson, Amplified Pressure Waves During Autoignition: Relevance to CAI Engines, 2002, p. 2868., 2002-01-, <https://www.sae.org/content/2002-01-2868/> (Accessed 26 September 2023).
- [7] P. Dai, Z. Chen, S. Chen, Y. Ju, Numerical experiments on reaction front propagation in n-heptane/air mixture with temperature gradient, *Proc. Combust. Inst.* 35 (2015) 3045–3052.
- [8] P. Dai, Z. Chen, X. Gan, Autoignition and detonation development induced by a hot spot in fuel-lean and CO<sub>2</sub> diluted n-heptane/air mixtures, *Combust. Flame* 201 (2019) 208–214.
- [9] J. Su, P. Dai, Z. Chen, Detonation development from a hot spot in methane/air mixtures: effects of kinetic models, *Int. J. Engine Res.* 22 (2021) 2597–2606.
- [10] Y. Gao, P. Dai, Z. Chen, Numerical studies on autoignition and detonation development from a hot spot in hydrogen/air mixtures, *Combust. Theory Model.* 24 (2020) 245–261.
- [11] H. Yu, C. Qi, Z. Chen, Effects of flame propagation speed and chamber size on end-gas autoignition, *Proc. Combust. Inst.* 36 (2017) 3533–3541.
- [12] A. Robert, S. Richard, O. Colin, T. Poinsot, LES study of deflagration to detonation mechanisms in a downsized spark ignition engine, *Combust. Flame* 162 (2015) 2788–2807.
- [13] M.B. Luong, H.G. Im, Prediction of the developing detonation regime in a NTC-fuel/air mixture with temperature inhomogeneities under engine conditions, *Proc. Combust. Inst.* 39 (2023) 4979–4988.
- [14] Z. Wang, Y. Qi, X. He, J. Wang, S. Shuai, C.K. Law, Analysis of pre-ignition to super-knock: hotspot-induced deflagration to detonation, *Fuel* 144 (2015) 222–227.
- [15] Y. Qi, Z. Wang, J. Wang, X. He, Effects of thermodynamic conditions on the end gas combustion mode associated with engine knock, *Combust. Flame* 162 (2015) 4119–4128.
- [16] W. Liu, Y. Qi, R. Zhang, Z. Wang, Flame propagation and auto-ignition behavior of iso-octane across the negative temperature coefficient (NTC) region on a rapid compression machine, *Combust. Flame* 235 (2022) 111688.
- [17] Z. Wang, Y. Qi, H. Liu, P. Zhang, X. He, J. Wang, Shock wave reflection induced detonation (SWRID) under high pressure and temperature condition in closed cylinder, *Shock Waves* 26 (2016) 687–691.
- [18] H. Yu, Z. Chen, End-gas autoignition and detonation development in a closed chamber, *Combust. Flame* 162 (2015) 4102–4111.
- [19] C. Qi, Z. Chen, Effects of temperature perturbation on direct detonation initiation, *Proc. Combust. Inst.* 36 (2017) 2743–2751.
- [20] M.T. Henry de Frahan, J.S. Rood, M.S. Day, H. Sitaraman, S. Yellapantula, B. A. Perry, R.W. Grout, A. Almgren, W. Zhang, J.B. Bell, J.H. Chen, PeleC: an adaptive mesh refinement solver for compressible reacting flows, *Int. J. High Perform. Comput. Appl.* 37 (2023) 115–131.
- [21] A.A. Konnov, Yet another kinetic mechanism for hydrogen combustion, *Combust. Flame* 203 (2019) 14–22.
- [22] Y. Morii, A.K. Dubey, H. Nakamura, K. Maruta, Two-dimensional laboratory-scale DNS for knocking experiment using n-heptane at engine-like condition, *Combust. Flame* 223 (2021) 330–336.
- [23] S. Desai, Y. Tao, R. Sivaramakrishnan, J.H. Chen, Effects of non-thermal termolecular reactions on wedge-induced oblique detonation waves, *Combust. Flame* (2023) 112681.
- [24] J.Y. Choi, F.H. Ma, V. Yang, Some numerical issues on simulation of detonation cell structures, *Combust. Explos. Shock Waves* 44 (2008) 560–578.
- [25] V. Raman, S. Prakash, M. Gamba, Nonidealities in rotating detonation engines, *Annu. Rev. Fluid Mech.* 55 (2023) 639–674.
- [26] Y. Sugiyama, Y. Nakayama, A. Matsuo, H. Nakayama, J. Kasahara, Numerical investigations on detonation propagation in a two-dimensional curved channel, *Combust. Sci. Technol.* 186 (2014) 1662–1679.
- [27] H. Nakayama, J. Kasahara, A. Matsuo, I. Funaki, Front shock behavior of stable curved detonation waves in rectangular-cross-section curved channels, *Proc. Combust. Inst.* 34 (2013) 1939–1947.
- [28] J.H. Lee, R. Knystautas, N. Yoshikawa, Photochemical initiation of gaseous detonations, *Acta Astronaut.* 5 (1978) 971–982.